Materials Transactions, Vol. 60, No. 9 (2019) pp. 2028 to 2032

Enhancement of Perpendicular Exchange Bias by Introducing Twin Boundary in Pt/Co/α-Cr_2O_3/α-V_2O_3 Epitaxial Film

Yu Shiratsuchi[1,*], Saori Yoshida[1], Satoshi Onoue[1], Chiharu Mitsumata[2], Nobuhito Inami[3], Tetsuro Ueno[4], Kanta Ono[5] and Ryoichi Nakatani[1]

[1]*Department of Materials Science and Engineering, Graduate School of Engineering, Osaka University, Suita 565-0871, Japan*
[2]*National Institute for Materials Science, Tsukuba 305-0047, Japan*
[3]*Nagoya University Synchrotron Radiation Research Center, Nagoya 464-8601, Japan*
[4]*Quantum Beam Science Research Directorate, National Institutes for Quantum and Radiological Science and Technology, Sayo-gun, Hyogo 679-5148, Japan*
[5]*Institute of Materials Structure Science, High Energy Accelerator Research Organization, Tsukuba 305-0801, Japan*

Perpendicular exchange anisotropy at the Co/α-Cr_2O_3 interface was investigated using the two types of films: the film with the single crystalline α-Cr_2O_3 and that with the twinned α-Cr_2O_3. Exchange anisotropy energy density J_K of the film with the single crystalline α-Cr_2O_3 was ∼0.09 erg/cm^2 whereas J_K of the film with the twinned α-Cr_2O_3 was ∼0.43 erg/cm^2, more than 4-times enhancement. We discussed the mechanism of the enhancement of J_K based on the exchange coupling at the twin boundary and that the spin frustration at the twin boundary can be the origin of the enhancement of J_K. [doi:10.2320/matertrans.MT-M2019102]

(Received April 1, 2019; Accepted June 13, 2019; Published August 2, 2019)

Keywords: *exchange anisotropy, Cr_2O_3, twin, spin frustration*

1. Introduction

Recent progress of the spintronics enabled us to control the antiferromagnetic (AFM) spin by an accessible external field such as spin current[1,2] and voltage.[3,4] Owing to the progress, the AFM spins has become the controllable functionality in the device. This is contractive to the long-term prejudge that the AFM material has been regarded to be as un-useless materials. Controlling the exchange bias polarity is one of the successive result of the AFM spin control.[4–8] This concept is based on that controlling the exchange bias polarity accompanies with the magnetization switching of the ferromagnetic (FM) layer at zero magnetic field[9] and obviously assumes that the exchange bias field H_{EX} is higher than the coercivity H_C. However, since the discovery of the exchange bias[10] and the successive application in the spintronic device,[11] the enhancement of H_{EX} in keeping low H_C is still a nontrivial problem because the appearance of H_{EX} sometimes accompanies with the coercivity enhancement.[12,13] Besides, since the recent spintronic device is designed so that the magnetization is perpendicular to the film plane, the high perpendicular exchange bias with the low H_C is desired. To achieve this, the basic research to elucidate the mechanism of the high exchange bias is essential. Further information on recent progress in the AFM spintronics can be found in the review, for example, by Jungwirth *et al.*[14] and Baltz *et al.*[15] and various theoretical and experimental works on the exchange bias have been reviewed in the previous reviews, for example, by Berkowitz and Takano,[16] Nogués and Schuller[17] and Stamps.[18]

Pt/Co/α-Cr_2O_3 film exhibits the high perpendicular exchange anisotropy J_K above 0.4 erg/cm^2 with the unique temperature dependence.[8,19,20] In this system, H_C can suppress below 50 Oe by using the suitable spacer layer.[21] Besides, we previously found that J_K could be enhanced by using the Pt buffer layer for the α-Cr_2O_3 growth instead of the direct growth on the α-Al_2O_3 substrate.[22] In the previous report, we discussed the enhancement of J_K based on the change in the magneto-crystalline anisotropy of α-Cr_2O_3 K_{AFM} caused by the lattice deformation and the specific ion positions of Cr^{3+} and O^{2-}. It was likely that the change in K_{AFM} was insufficient to explain the large enhancement of J_K by itself and was suggested that the microstructure such as the grain boundary was necessary to be taken into consideration. In order to address the inherent effect of the microstructure eliminating the difference in the crystal parameters (lattice parameters and specific ion positions), the fabrication of the α-Cr_2O_3 layer on the same buffer layer is suitable. In this paper, we examined the effect of the twin boundary on J_K by suitably controlling crystalline quality of the α-Cr_2O_3 layer prepared on the same buffer layer: the single-crystalline film or the twinned film.

To fabricate the single crystalline α-Cr_2O_3, the buffer layer with the same crystal structure, the corundum structure is suitable. The direct deposition on the α-Al_2O_3 substrate is one of the way to obtain the single-crystalline α-Cr_2O_3 as in our previous paper.[22] Based on this principle, α-V_2O_3 was used as one of the candidates for the buffer layer. In this case, however, the twinned α-Cr_2O_3 is difficult to be grown. In order to obtain the twinned α-Cr_2O_3 on the α-V_2O_3 buffer layer, it is needed to introduce the twin boundary in the α-V_2O_3 layer and to do so, the twinned Pt(111) seed layer was used. Based on these considerations, we adopted two types of underlayers to obtain the single-crystalline and twinned α-Cr_2O_3 layers: the single-crystalline α-V_2O_3-buffer/α-Al_2O_3-sbst. for the single-crystalline α-Cr_2O_3 and the twinned α-V_2O_3-buffer/Pt-seed/α-Al_2O_3-sbst. for the twinned α-Cr_2O_3, respectively.

It should be additionally noted that for the above scenario, the α-Al_2O_3 buffer layer (not a substrate) is another candidate

*Corresponding author, E-mail: shiratsuchi@mat.eng.osaka-u.ac.jp

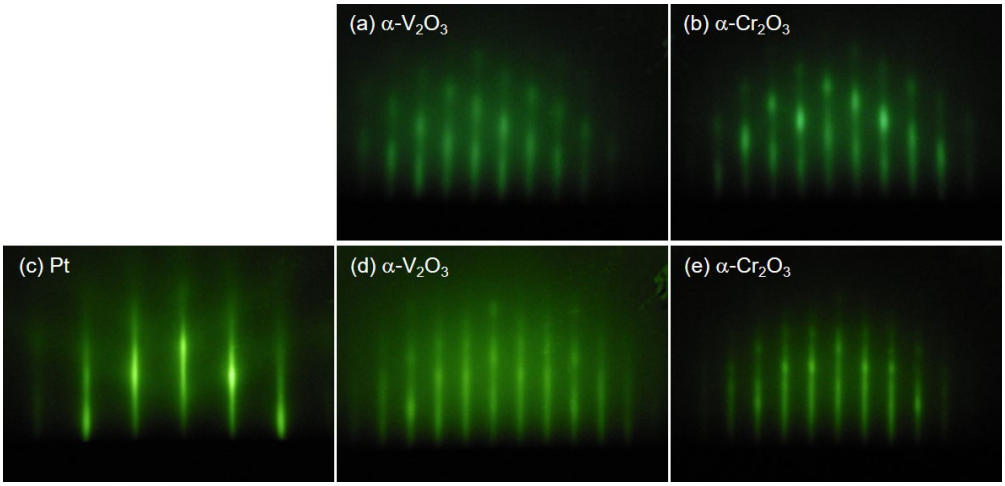

Fig. 1 $[11\bar{2}0]_{\alpha\text{-Al2O3}}$-azimuthal RHEED patterns of α-V_2O_3, α-Cr_2O_3 and Pt buffer layer. Top and bottom images represent the RHEED pattern for the films without and with the Pt buffer layer, respectively.

instead of α-V_2O_3. As well known, α-Cr_2O_3 is a proto-typical magnetoelectric (ME) material and the AFM domain state can be controlled by the ME field.[4–8] Hence, keeping in mind the ME control of the AFM spin/domain, the conductive underlayer is more prominent for the application, and thus the conductive α-V_2O_3 was employed in this paper; the ME control of the AFM domain is, however, beyond the scope of this paper.

2. Experimental

DC magnetron sputtering system with a base pressure below 5×10^{-7} Pa was used for the film fabrication. Stacking structure of the films were Pt(5 nm)/Co(0.8 nm)/α-Cr_2O_3(150 nm)/α-V_2O_3(20 nm)/Pt(0, 20 nm) on the α-Al_2O_3(0001) substrate; two types of films, i.e., with and without the Pt buffer layer, were fabricated to alter the single-crystalline and the twinned α-Cr_2O_3/α-V_2O_3 layers (see Fig. 1). The Pt buffer layer was deposited at 873 K. α-V_2O_3 and α-Cr_2O_3 layers were deposited at 773 K by means of the reactive sputtering technique using the Ar and O_2 gas mixture. The Co and Pt capping layers were deposited at room temperature. The crystal structure of each layer was checked by reflection high-energy electron diffraction (RHEED) and synchrotron X-ray diffraction (XRD) measurements. RHEED chamber was connected to the deposition chamber via ultrahigh vacuum and thus, the RHEED observations were done without exposing the sample to air. The synchrotron XRD measurements were carried out at BL-8B beamline at the Photon Factory of KEK for the film without Pt buffer layer to check the crystallographic phase of the V oxide layer and the Cr oxide layer. X-ray energy was set to 18 keV. For the synchrotron XRD measurements, Pt(5)/Co(0.8)/α-Cr_2O_3(30)/α-V_2O_3(20) stacked film on the α-Al_2O_3(0001) substrate was used.

Magnetic properties were characterized by using vibrating sample magnetometer for the magnetization curve at room temperature and magneto-optic Kerr effect (MOKE) for the temperature dependence of H_{EX} and H_C. The MOKE measurements were carried out with the polar configuration where the magnetic field was applied to the direction perpendicular to the film. The measurement temperature of the MOKE was varied from 80 K to 300 K. To access the low temperature, the sample was cooled from 310 K, above the Néel temperature of α-Cr_2O_3 (307 K for the bulk α-Cr_2O_3[23]) under the magnetic field of -4 kOe, i.e. the field-cooling. The exchange anisotropy energy density J_K (erg/cm^2) was calculated using the saturation magnetization per unit area, $M_S * t_{FM}$ (emu/cm^2) and H_{EX} (Oe) as[16–18]

$$J_K = M_S * t_{FM} * H_{EX} \quad (1)$$

3. Results and Discussions

Figure 1 shows the RHEED images of two types of films. The RHEED pattern of the V oxide layer directly grown on the α-Al_2O_3(0001) substrate (Fig. 1(a)) and the Cr oxide (Fig. 1(b)) were asymmetric with respect to the (0,0) streak. The very similar diffraction patterns from two layers indicate the epitaxial growth. The asymmetric RHEED pattern is a signature of the 3-fold symmetry of the in-plane atom arrangement. The candidates are the single-crystalline rock-salt (111) such as VO(111) or the single-crystalline corundum (0001) such as α-V_2O_3(0001) and α-Cr_2O_3(0001). According to the synchrotron XRD pattern shown in Fig. 2, the diffraction patterns from the V–O phase and the Cr–O phase are same as those from the α-Al_2O_3(0001) substrate. Since the α-Al_2O_3 has the corundum structure, this matching of the diffraction patterns indicates that the V oxide and the Cr oxide are α-V_2O_3(0001) and α-Cr_2O_3(0001), respectively.

In contrast to the asymmetric patterns, the RHEED patterns of the α-V_2O_3 layer (Fig. 1(d)) and the α-Cr_2O_3 layer (Fig. 1(e)) grown on the Pt-buffered α-Al_2O_3(0001) substrate are symmetric with respect to the (0,0) streak. This is because the α-V_2O_3 layer and the α-Cr_2O_3 layer was grown on the 6-fold symmetric twinned Pt(111) (shown in Fig. 1(c)) in an epitaxial manner. Namely, the symmetric pattern is caused by the superimposed diffractions of the twinned crystal. Because the symmetric pattern was observed in the $[11\bar{2}0]$-azimuth,

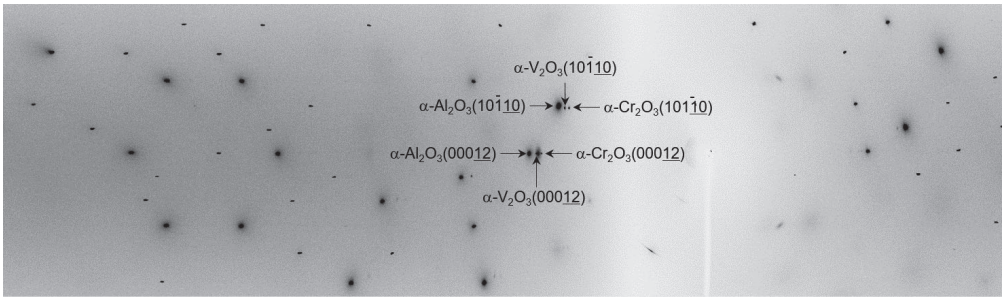

Fig. 2 Two-dimensional XRD pattern of Pt/Co/α-Cr_2O_3/α-V_2O_3 stacked film on the α-Al_2O_3(0001) substrate. The incident angle of X-ray was 20°–25°.

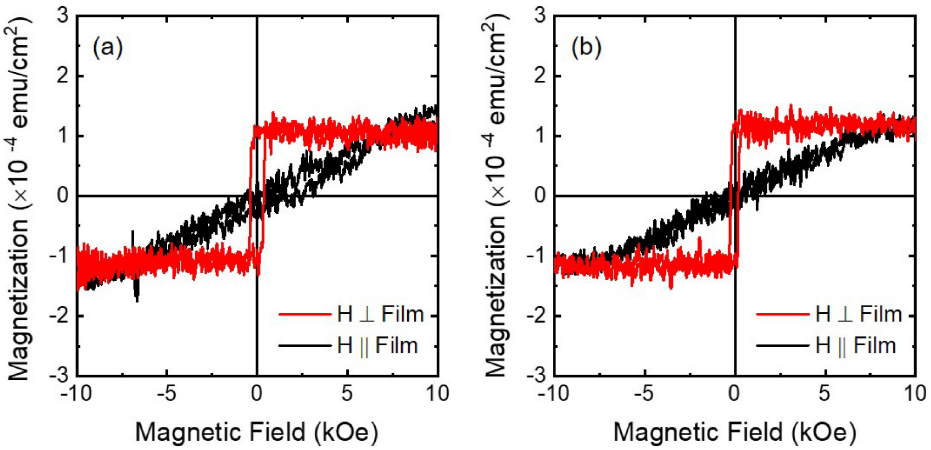

Fig. 3 Magnetization curves measured at room temperature for the films (a) without and (b) with the Pt buffer layer. Red and black curves represent out-of-plane and in-plane curves, respectively.

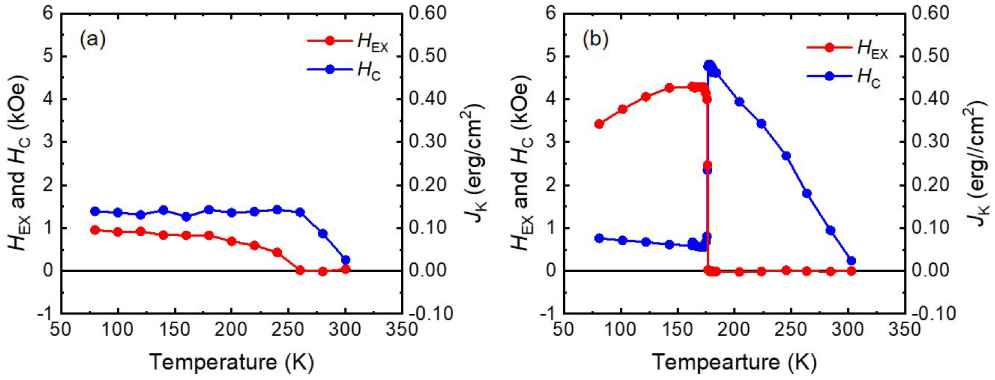

Fig. 4 Temperature dependence of exchange bias field H_{EX} (red circle, left axis), J_K (red circle, right axis) and coercivity H_C (blue circle, left axis) for the films with (a) without and (b) with the Pt buffer layer, respectively. On the right axis, the exchange magnetic anisotropy energy density J_K, calculated using H_{EX} was shown.

the twin boundary is parallel to [11$\bar{2}$0]. Note that because of the symmetry of the corundum structure, the twin boundaries parallel to [10$\bar{1}$0] are also included in the film.

Figure 3 shows the magnetization curve measured at room temperature. For both films, the saturation field was zero in the direction perpendicular to the film whereas the in-plane magnetization is saturated at ~10 kOe; the uniaxial magnetic anisotropy energy density is similar for both films. The saturation magnetization per unit area $M_S * t_{FM}$ is also similar for both films, $\sim 1.0 \times 10^{-4}$ emu/cm^2, which was used for the estimation of J_K using eq. (1). It should be noted that the determination of the uniaxial magnetic anisotropy energy density is difficult because the precise value of the saturation magnetization M_S is difficult to be determined because of the spin polarization of Pt.[21,24)]

Figure 4 shows the temperature dependence of H_{EX} and H_C. For the film with the single crystalline α-Cr_2O_3 layer (Fig. 4(a)), H_{EX} appears below 260 K and gradually increase with decreasing temperature and becomes almost constant below 180 K. H_{EX} reaches ~0.95 kOe at 80 K, which results in $J_K \sim 0.09$ erg/cm^2. H_C gradually increases with decreasing temperature and is almost constant below 260 K at 1.3–

1.4 kOe. The reduction of H_C toward 300 K is probably relevant to the depression of the effective magnetic anisotropy energy toward the Néel temperature[25] (307 K for the bulk α-Cr_2O_3[23]).

Temperature dependence of H_{EX} and H_C was drastically different for the film with the twinned α-Cr_2O_3 layer. In the temperature range of 180–300 K, H_{EX} stays zero while H_C increases monotonically from 0.23 kOe to 4.9 kOe. At 176 K, H_{EX} abruptly appears. Accompanied with the abrupt onset of H_{EX}, H_C decreases at the same temperature. H_{EX} reaches maximum at about 170 K and decreases again with decreasing temperature. The reduction of H_{EX} in the low temperature regime is due to the spin canting of the interfacial Cr^{3+} ions from the surface normal.[5] The highest H_{EX}, 4.3 kOe was obtained at 170 K yielding the highest $J_K \sim 0.43$ erg/cm^2.

The blocking temperature T_B at which H_{EX} becomes zero is different for the two types of films. The highly different temperature dependence of H_{EX} suggests that the blocking mechanism is different for the two types of films. Namely, the direct quantitative comparison of T_B may be difficult. Instead, here we discuss the possible blocking mechanisms for the films.

For the case of the film with the single-crystalline α-Cr_2O_3 layer, the relative length of the magnetic domain wall width $\delta_W \propto {K_{AFM}}^{-1/2}$ in the α-Cr_2O_3 layer with respect to the α-Cr_2O_3 thickness t_{AFM} may dominate the blocking phenomenon. According to the temperature dependence of K_{AFM} for the bulk α-Cr_2O_3,[23] K_{AFM} gradually decrease above 200 K. Resultantly, δ_W gradually increases and exceeds t_{AFM} above T_B. When $\delta_W \gg t_{AFM}$, the magnetic domain wall cannot be pinned anymore and H_{EX} disappears.

In contrast, for the case of the film with the twinned α-Cr_2O_3 layer, H_{EX} abruptly onsets implying that some energy competition rather than the thermal agitation plays a key role. This adiabatic mechanism is qualitatively explained by the Meiklejohn and Beans' exchange anisotropy model (M-B model).[10] Based on this model, the onset of the exchange bias is expressed by the criteria

$$\frac{K_{AFM} \cdot t_{AFM}}{J} \geq 1 \qquad (2)$$

where J denotes the interfacial exchange coupling energy, which is proportional to J_K in the framework of the M-B model. On the basis of eq. (2), the temperature dependences of J and K_{AFM} determine T_B. The details of this mechanism can be found in our previous overview.[8] It should be noted that the above mentioned blocking mechanisms are contractive to that for the other general system where T_B is determined by the thermal agitation of the AFM moment. This difference is probably due to the typical value of t_{AFM} adopted: typically >50 nm in our system and <10 nm in the other system such as FM/Mn-based AFM layer.[16–18]

Another important notice in Fig. 4 is more than four times enhancement of J_K in the films with the twinned α-Cr_2O_3. As described in the introduction, it was likely that the lattice deformation and the resultant change in K_{AFM} were insufficient to explain the phenomena by itself. Here we discuss the enhancement of J_K from the viewpoint of the spin frustration at the twin boundary. As discussed in the FM/Mn–Ir system,[26] the non-collinear spin structure can be the origin of the high exchange bias. In the presence of the spin frustration, the spin orientation can be altered from the original direction and resultantly the spin structure becomes non-collinear. According to this model, even in the originally collinear spin structure such as α-Cr_2O_3, the spin frustration and the non-collinear spin structure can be induced by introducing the magnetic domain wall. In our case, the twin boundary can induce the spin frustration as discussed below. In the following discussion, the exchange coupling between Cr^{3+} ions are assumed to be similar to the bulk α-Cr_2O_3.[27]

In Fig. 5, the atom arrangement around the twin boundary along $[11\bar{2}0]$ of α-$Cr_2O_3(0001)$ layer are schematically shown. For the case of the single-crystalline α-Cr_2O_3 (Fig. 5(a)), on the $[11\bar{2}0]$ projection, each Cr^{3+} atom, for example Cr^{3+} labelled as 0 (notated as $Cr^{3+}(0)$) interacts antiferromagnetically with $Cr^{3+}(1)$ through J_1 and with $Cr^{3+}(3, 1')$ through J_2. Since the exchange coupling between $Cr^{3+}(1)$ and $Cr^{3+}(3, 1')$ and that between $Cr^{3+}(3)$ and $Cr^{3+}(3')$ are both ferromagnetic, i.e. J_4 and J_6, respectively, the spin frustration does not come up. On the other hand, on the twin boundary (Fig. 5(b)), the atom arrangement is mirror-symmetric with respect to the twin boundary. In this case, $Cr^{3+}(0)$ antiferromagnetically couples with $Cr^{3+}(3)$ and $Cr^{3+}(3')$ through J_2. Besides, the distance between $Cr^{3+}(3)$ and $Cr^{3+}(3')$ is same as the nearest neighbor Cr^{3+} ions, $Cr^{3+}(0)$–$Cr^{3+}(1)$, which should yield the AFM exchange coupling J_1, denoted as quasi-J_1 in Fig. 5(b). According to Ref. 27), the strength of J_1 and J_2 are comparable, and consequently, on the $Cr^{3+}(0)$–$Cr^{3+}(3)$–$Cr^{3+}(3')$ triangle, the spins are strongly frustrated. The similar spin frustration can be induced on $Cr^{3+}(1)$–$Cr^{3+}(3)$–$Cr^{3+}(3')$, $Cr^{3+}(1)$–$Cr^{3+}(4)$–$Cr^{3+}(4')$ triangles. The exchange coupling between $Cr^{3+}(1)$ and $Cr^{3+}(3, 3')$ and that between $Cr^{3+}(1)$ and $Cr^{3+}(4, 4')$ are J_3 and J_4, respectively. J_3 and J_4 are two-order smaller than J_1 and J_2.[27] Hence, the spin frustration on the latter two triangles should not be so strong. For the quantitative understanding, the theoretical verification is beneficial and it will be investigated in near future.

4. Summary

We report the enhancement of J_K at the Co/α-Cr_2O_3 interface by introducing the twin boundary in the α-Cr_2O_3 layer. J_K for the film with the single-crystalline α-Cr_2O_3 was at most 0.09 erg/cm^2 whereas J_K for the film with the twinned α-Cr_2O_3 was enhanced more than four times, $\sim$0.43 erg/cm^2. As the possible origin of this enhancement, we proposed the spin frustration at the twin boundary. This result suggest that J_K can be controlled by the microstructure and the grain-boundary engineering.

Acknowledgements

The synchrotron experiments were carried out with the approval of KEK as a proposal (Grant No. 2013V001). This work was partly supported by JSPS KAKENHI (Project Nos. 16H03832, 16H02389, and 18K18311).

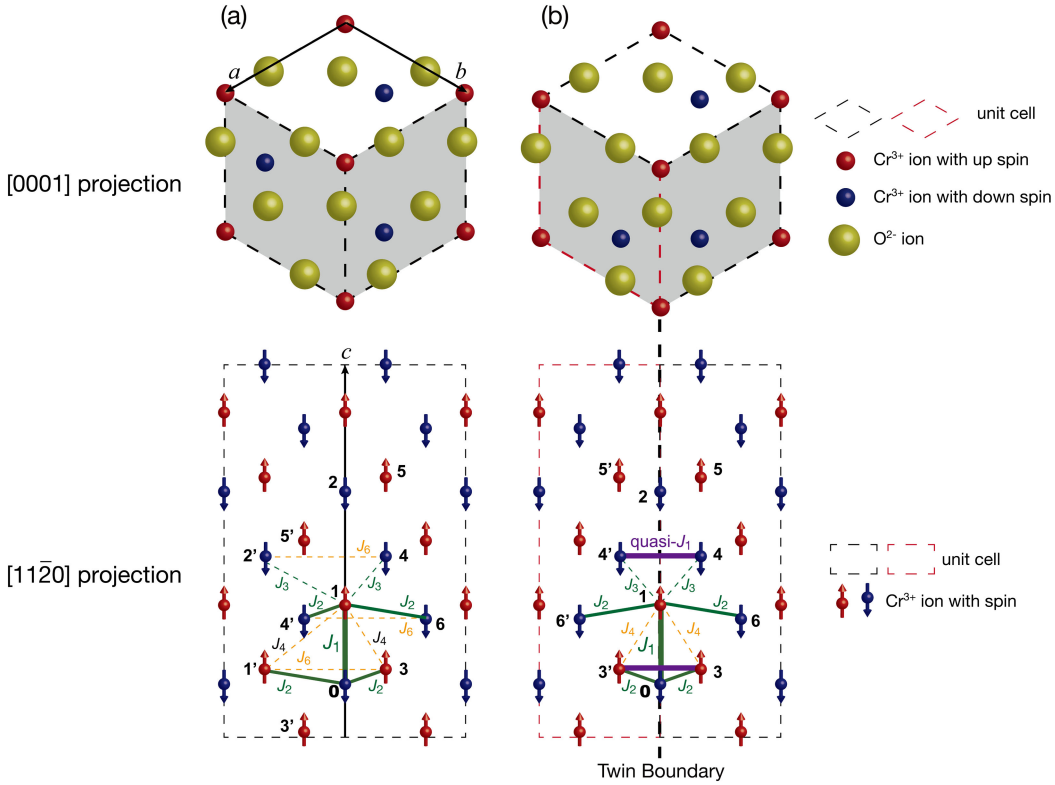

Fig. 5 Schematic representation of the atom arrangement of the α-Cr_2O_3(0001) (a) without and (b) with the twin boundary. Top and bottom drawings represent the [0001] and [11$\bar{2}$0] projected atom arrangement, respectively. In the [0001] projection, the top three layers, i.e. Cr^{3+}–O^{2-}–Cr^{3+} layer are drawn. In the [11$\bar{2}$0] projection, the Cr^{3+} ions within the hatched units in (a) are shown. Thin dotted lines represent the unit cell. Red and blue circles represent the Cr^{3+} ions with up and down spins, respectively, and yellow circle represent the O^{2-} ions. Solid lines in the bottom drawings represent the exchange coupling between Cr^{3+} ions. Orange and green lines represent the FM and AFM coupling, respectively. Purple line in (b) represents the AFM coupling through the quasi-J_1 (see text). The notation of J_i ($i = 1$–6) is same as the Ref. 27). Line thickness qualitatively reflects the coupling strength.

REFERENCES

1) A.S. Núñez, R.A. Duine, P. Haney and A.H. MacDonald: Phys. Rev. B **73** (2006) 214426.
2) T. Moriyama, K. Oda, T. Ohkochi, M. Kimata and T. Ono: Sci. Rep. **8** (2018) 14167.
3) Y.-H. Chu *et al.*: Nat. Mater. **7** (2008) 478.
4) P. Borisov, A. Hochstrat, X. Chen, W. Kleeman and C. Binek: Phys. Rev. Lett. **94** (2005) 117203.
5) X. He, Y. Wang, N. Wu, A.N. Caruso, E. Vescovo, K.D. Belashchenko, P.A. Dowben and C. Binek: Nat. Mater. **9** (2010) 579, and supplemental information.
6) T. Ashida, M. Oida, N. Shimomura, T. Nozaki, T. Shibata and M. Sahashi: Appl. Phys. Lett. **104** (2014) 152409.
7) K. Toyoki, Y. Shiratsuchi, T. Nakamura, C. Mitsumata, S. Harimoto, Y. Takechi, T. Nishimura, H. Nomura and R. Nakatani: Appl. Phys. Express **7** (2014) 114201.
8) X. Chen, A. Hochstrat, P. Borisov and W. Kleemann: Appl. Phys. Lett. **89** (2006) 202508.
9) Y. Shiratsuchi and R. Nakatani: Mater. Trans. **57** (2016) 781.
10) W.H. Meiklejohn and C.P. Bean: Phys. Rev. **102** (1956) 1413.
11) B. Dieny, V.S. Speriosu, S. Metin, S.S.P. Parkin, B.A. Gurney, P. Baumgart and D.R. Wilhoit: J. Appl. Phys. **69** (1991) 4774.
12) C. Leighton, J. Nogués, B.J. Jönsson-Åkermann and I.K. Schuller: Phys. Rev. Lett. **84** (2000) 3466.
13) T. Gredig, I.N. Krivorotov, P. Eames and E.D. Dahlberg: Appl. Phys. Lett. **81** (2002) 1270.
14) T. Jungwirth, X. Marti, P. Wadley and J. Wunderlich: Nat. Nanotechnol. **11** (2016) 231.
15) V. Baltz, A. Manchon, M. Tsoi, T. Moriyama, T. Ono and Y. Tserkovnyak: Rev. Mod. Phys. **90** (2018) 015005.
16) A.E. Berkowitz and K. Takano: J. Magn. Magn. Mater. **187** (1999) 105.
17) J. Nogués and I.K. Schuller: J. Magn. Magn. Mater. **192** (1999) 203.
18) R.L. Stamps: J. Phys. D **33** (2000) R247.
19) Y. Shiratsuchi, T. Fujita, H. Oikawa, H. Noutomi and R. Nakatani: Appl. Phys. Express **3** (2010) 113001.
20) Y. Shiratsuchi, Y. Takechi, K. Toyoki, Y. Nakano, S. Onoue, C. Mitsumata and R. Nakatani: Appl. Phys. Express **6** (2013) 123004.
21) Y. Shiratsuchi, W. Kuroda, T.V.A. Nguyen, Y. Kotani, K. Toyoki, T. Nakamura, M. Suzuki, K. Nakamura and R. Nakatani: J. Appl. Phys. **121** (2017) 073902.
22) Y. Shiratsuchi, Y. Nakano, N. Inami, T. Ueno, K. Ono, R. Kumai, R. Sagayama and R. Nakatani: J. Appl. Phys. **123** (2018) 103903.
23) S. Foner: Phys. Rev. **130** (1963) 183.
24) M. Suzuki, H. Muraoka, N. Ishimatsu, Y. Isohama and Y. Sonobe: Phys. Rev. B **72** (2005) 054430.
25) T. Nozaki, M. Oida, T. Ashida, N. Shimomura and M. Sahashi: Appl. Phys. Lett. **103** (2013) 242418.
26) C. Mitsumata, A. Sakuma and K. Fukamichi: Phys. Rev. B **68** (2003) 014437.
27) E.J. Samuelson, M.T. Hutchings and G. Shirane: Physica **48** (1970) 13.